Transformation and Upwelling of Bottom Water in Fracture Zone Valleys

A. M. THURNHERR

Lamont-Doherty Earth Observatory, Palisades, New York

L. CLÉMENT

National Oceanography Centre, Southampton, United Kingdom

L. ST. LAURENT

Woods Hole Oceanographic Institution, Woods Hole, Massachusetts

R. FERRARI

Massachusetts Institute of Technology, Cambridge, Massachusetts

T. IJICHI

Woods Hole Oceanographic Institution, Woods Hole, Massachusetts

ABSTRACT

Closing the overturning circulation of bottom water requires abyssal transformation to lighter densities and upwelling. Where and how buoyancy is gained and water is transported upward remain topics of debate, not least because the available observations generally show downward-increasing turbulence levels in the abyss, apparently implying mean vertical turbulent buoyancy-flux divergence (densification). Here, we synthesize available observations indicating that bottom water is made less dense and upwelled in fracture zone valleys on the flanks of slow-spreading midocean ridges, which cover more than one-half of the seafloor area in some regions. The fracture zones are filled almost completely with water flowing up-valley and gaining buoyancy. *Locally,* valley water is transformed to lighter densities both in thin boundary layers that are in contact with the seafloor, where the buoyancy flux must vanish to match the no-flux boundary condition, and in thicker layers associated with downward-decreasing turbulence levels below interior maxima associated with hydraulic overflows and critical-layer interactions. *Integrated across the valley*, the turbulent buoyancy fluxes show maxima near the sidewall crests, consistent with net convergence below, with little sensitivity of this pattern to the vertical structure of the turbulence profiles, which implies that buoyancy flux convergence in the layers with downward-decreasing turbulence levels dominates over the divergence elsewhere, accounting for the net transformation to lighter densities in fracture zone valleys. We conclude that fracture zone topography likely exerts a controlling influence on the transformation and upwelling of bottom water in many areas of the global ocean.

1. Introduction

Antarctic Bottom Water (AABW) fills all major ocean basins below approximately 3500 m. At these depths the large-scale seafloor topography away from the continents is dominated by midocean ridges that separate the oceans into abyssal basins (Fig. 1). Most of the global midocean ridge system, with a total axial length of approximately 60 000 km—1.5 times the circumference of Earth—is associated with seafloor spreading. The regional morphology of the ridges varies systematically with the spreading rate of the underlying tectonic plates. The flanks of slow-spreading ridges, which account for $\frac{2}{3}$ of the global crest length, are corrugated by quasi-regularly spaced fracture zone (FZ)

ⓐ Denotes content that is immediately available upon publication as open access.

Corresponding author: A. M. Thurnherr, ant@ldeo.columbia.edu

FIG. 1. Seafloor topography of parts of the Atlantic and Indian Oceans. Basin-scale topography is dominated mostly by slow-spreading midocean ridges, the flanks of which are corrugated by fracture zone valleys that are typically 1000 m deep and often exceed 1000 km in length. Magenta and cyan symbols show the hydrographic stations in the two FZs shown later in Fig. 3, one on the MAR and the other on the Southeast Indian Ridge.

valleys (the dark striations in the figure) that result from the axial segmentation of the ridges. These FZ valleys slope upward toward the midocean ridge crests, and most of them terminate at depths shallower than 3500 m as they are blocked by the sidewalls of the median valleys that are also associated with slow seafloor spreading rates. Most FZs therefore do not provide unobstructed cross-ridge pathways for AABW. In the Atlantic and Indian Oceans, the corrugated flanks of slow-spreading midocean ridges account for approximately one-half of the total seafloor area (Fig. 1). In the South Atlantic, the valleys are spaced approximately every 100 km along the ridge flanks, are bounded by lateral walls that typically rise approximately 1000 m above the valley floors, and most of the FZs extend more than 1000 km off axis. Since the slow-spreading MORs in other regions are topographically similar (Fig. 1), we use these scales to estimate the total length of FZ valleys globally as 7×10^5 km—nearly 2 times the Earth–moon distance.

Bottom waters are continuously exported from several formation regions around the Antarctic continent, implying mean upwelling (upward vertical transport) from the deepest layers of all ocean basins. In the Brazil basin in the western South Atlantic, bottom water is transported eastward and upward in the approximately 30 FZ valleys that corrugate the western flank of the Mid-Atlantic Ridge (MAR) between the equator and 30°S (St. Laurent et al. 2001b; Thurnherr and Speer 2003). The amount of upwelling in the FZ valleys is sufficient to balance the entire AABW flowing into this basin from the south (St. Laurent et al.

2001b; Morris et al. 2001; Clément et al. 2017). In addition to upwelling there must also be a mean buoyancy gain (i.e., a decrease in density) along the path of the AABW in order for a quasi-steady state to be maintained. Since AABW is not in contact with the atmosphere anywhere outside its formation regions, the required buoyancy must be derived from a combination of geothermal heating across the sea floor and turbulent mixing with overlying waters. While turbulent mixing in stable stratification is associated with consistently downward flux of buoyancy, it is the divergence of this flux that determines whether a water parcel loses or gains buoyancy (e.g., Polzin et al. 1997). Except in very weak stratification the local convergence of buoyancy flux in the ocean interior is related to vertical gradients in turbulent dissipation ε, with upward-increasing turbulence levels ($\partial \varepsilon / \partial z > 0$) required for local buoyancy gain.

Two pioneering microstructure surveys from the South Atlantic, carried out in the context of the Brazil Basin Tracer Release Experiment (BBTRE) in the 1990s, revealed high levels of turbulence (relative to the "oceanic background" levels observed over the adjacent abyssal plain) over the western flank of the MAR (Polzin et al. 1997; Ledwell et al. 2000; St. Laurent et al. 2001b), with the strongest turbulence occurring inside FZ valleys (St. Laurent et al. 2001a,b; Thurnherr et al. 2005). In order to investigate the processes causing elevated turbulence in FZ valleys in greater detail, a particular FZ near 21°S that was particularly well sampled during the BBTRE (magenta bullets in Fig. 1) was revisited more recently during the DoMORE

project (Clément et al. 2017; Zhao and Thurnherr 2018; Clément and Thurnherr 2018). While the magnitude of the turbulent buoyancy fluxes observed over the MAR flank in the Brazil basin is sufficient to account for the observed consumption of AABW (Morris et al. 2001), it is not immediately clear how to reconcile the required transformation to lighter densities with an apparent predominance of downward-increasing turbulence ($\partial\varepsilon/\partial z < 0$) in the observations (Polzin et al. 1997; St. Laurent et al. 2001b). Plausible solutions that have been proposed to solve this conundrum include decoupling of the buoyancy fluxes from turbulence levels in weakly stratified bottom boundary layers (St. Laurent et al. 2001b), insufficient sampling of hydraulic processes in FZ valleys (Thurnherr et al. 2005), lack of sampling near the seabed where turbulent buoyancy fluxes must vanish (Ferrari et al. 2016; McDougall and Ferrari 2017), as well as incorrectly inferred vertical gradients in the mean turbulence levels caused by averaging in height-above-bottom coordinates (Clément and Thurnherr 2018). It has also been argued that hypsography provides an independent constraint on the area integrated buoyancy flux in topographically constrained regions (e.g., Armi 1979; Klocker and McDougall 2010; Kunze et al. 2012). Of particular relevance for bottom water transformation in FZ valleys is the work of Kunze et al. (2012) who consider cross-valley integrated water-mass transformation in shelf-slope canyons. They show that in downward-narrowing valleys the cross-valley integrated buoyancy flux is convergent, even if individual vertical dissipation profiles have no vertical gradients outside thin, well mixed boundary layers that are in physical contact with the seabed. It is tempting to read this as implying that waters become lighter in the net, even though the buoyancy flux is divergent (or has zero vertical gradient) everywhere, in apparent contradiction with the arguments based on buoyancy conservation. In the present work, we generalize the model of Kunze et al. (2012) 1) by explicitly considering the bottom boundary layer where the turbulent buoyancy flux across the seabed must vanish, 2) by including the effects of the observed vertical gradients in the turbulent buoyancy fluxes, and 3) by considering the hypsographic constraints imposed by realistic FZ topography. In section 4 we discuss the apparently contradictory conclusions derived from buoyancy conservation and from hypsographic arguments in this setting.

2. Fracture zone hydrography and circulation

Figure 2 shows a 200-km-long stretch of FZ topography near 21°S in the western South Atlantic that was sampled both during the BBTRE and DoMORE projects (section 1). In this region the mean depth of the valley thalweg is approximately 4500 m and the mean sidewall depth is around 3500 m; that is, the valley is approximately 1000 m deep. In the along-FZ direction the topographic roughness is dominated by quasi-regular meridionally oriented ridges with horizontal wavelengths on the order of 10 km and vertical scales of hundreds of meters. These topographic structures are called abyssal hills—they are intrinsically associated with seafloor spreading and they strike parallel to the midocean ridge spreading axis; that is, they are approximately perpendicular to the FZ valleys. Abyssal hills constrict the FZs both vertically and laterally, separating the valley floor into a sequence of comparatively deep and wide basins, connected by sills and narrows, some of which host hydraulically controlled overflows (Thurnherr et al. 2005; Clément et al. 2017). Note that the abyssal hills have significantly greater vertical relief inside the valley along the sidewalls than along the thalweg—between 500 and 1000 m along the northern sidewall versus 100–300 m along the thalweg in the region shown in Fig. 2 (inset panel)—and along the crests of the sidewalls (150 m; Polzin 2009).

During a survey in 1997, a 900-km-long section of CTD and microstructure profiles was occupied along the thalweg of the 21°S FZ, with additional profiles collected in neighboring valleys (St. Laurent et al. 2001b). Moored instruments deployed in 1996 in the middle of the valley near 17°45′E recorded velocities and temperatures in and above the FZ for two years (Thurnherr et al. 2005; Toole 2007). During the recent DoMORE project, a section of the same FZ valley (between 13° and 17°E) was surveyed again, and moorings were deployed in an overflow at 14°45′E, as well as approximately 100 km farther east near 13°45′E (Clément et al. 2017). The consistent mean eastward flow of AABW down the large-scale along-valley density gradient in the bottom 500 m that is apparent in these data (Fig. 3, left panel) provides unambiguous evidence for lightening and upwelling of bottom water inside this FZ (Fig. 3, left panel). Since the valley is sloping upward toward the MAR crest (near 11°30′W), the mean eastward flow is associated with net upwelling. Using a representative along-valley velocity away from overflows of $0.02\,\mathrm{m\,s^{-1}}$ (Thurnherr et al. 2005; Clément et al. 2017) yields a mean upwelling velocity of approximately $2 \times 10^{-5}\,\mathrm{m\,s^{-1}}$ for the region between the BBTRE mooring near 18°W (4875-m water depth) and the eastern DoMORE mooring near 13°45′W (4400-m water depth).

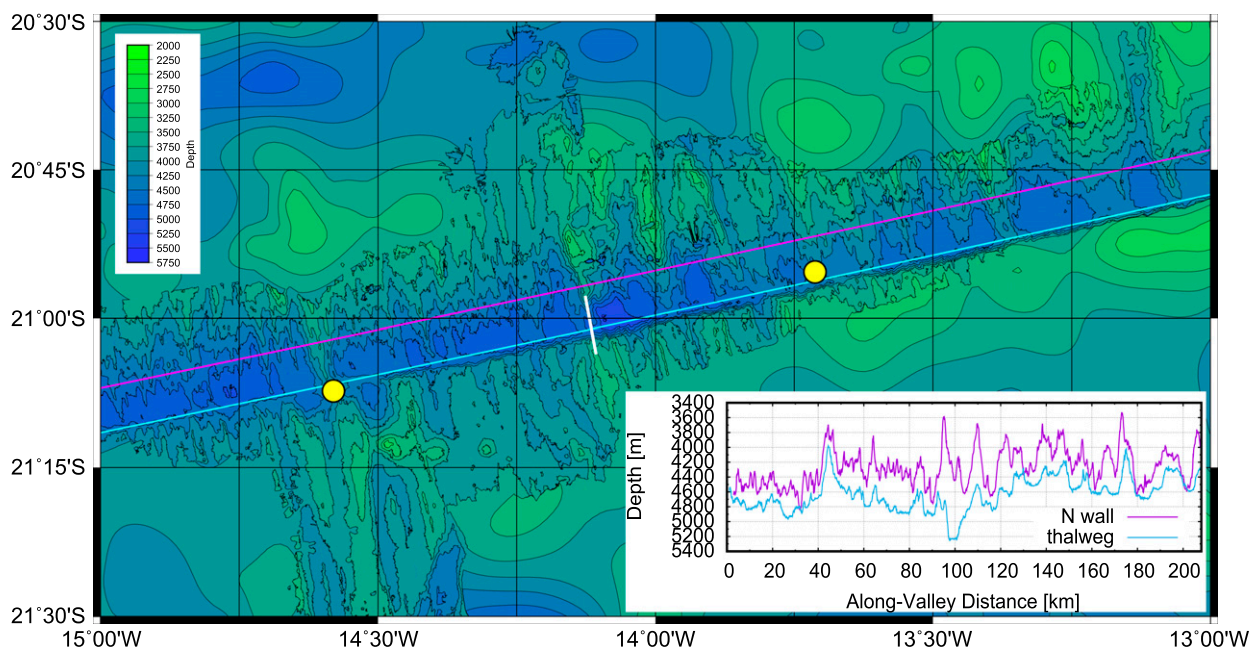East of 14°30′W the rising flank of the MAR confines the interface between AABW and overlying North

FIG. 2. Topography map of a 200-km-long section of the South Atlantic FZ shown below in Fig. 3; ETOPO-1 data are used in the areas without multibeam coverage. Yellow symbols show locations of the DoMORE moorings used in Figs. 3 and 4, below; cyan and magenta lines show the tracks of the depth sections in the inset plot; the white line shows the location of the valley cross section shown later in Fig. 5. Inset: Depth sections along the valley thalweg and along the base of the northern sidewall approximately 8 km north of the thalweg.

Atlantic DeepWater (NADW) inside the FZ valley. Therefore, the approximately 0.1 Sv ($1\,\mathrm{Sv} \equiv 10^6\,\mathrm{m^3\,s^{-1}}$) of AABW that flows eastward across the DoMORE sill (Clément et al. 2017) is entirely consumed (transformed into less dense water) and vertically transported to depths shallower than 3900 m within the valley. As this transformed and upwelled bottom water is still confined within the FZ it must leave the valley in a westward current, consistent with the DoMORE mooring observations. The mean upwelling velocity

east of the DoMORE sill that is implied by this interpretation—approximately $2.5 \times 10^{-5}\,\mathrm{m\,s^{-1}}$, using a mean valley width of approximately 20 km at 3900 m (Fig. 2)—is similar to the estimated mean upwelling velocity between the BBTRE and DoMORE moorings. Further support for this interpretation is provided by the observation that the eastward along-valley transport is reduced by approximately 50% between the two DoMORE mooring sites (Clément et al. 2017).
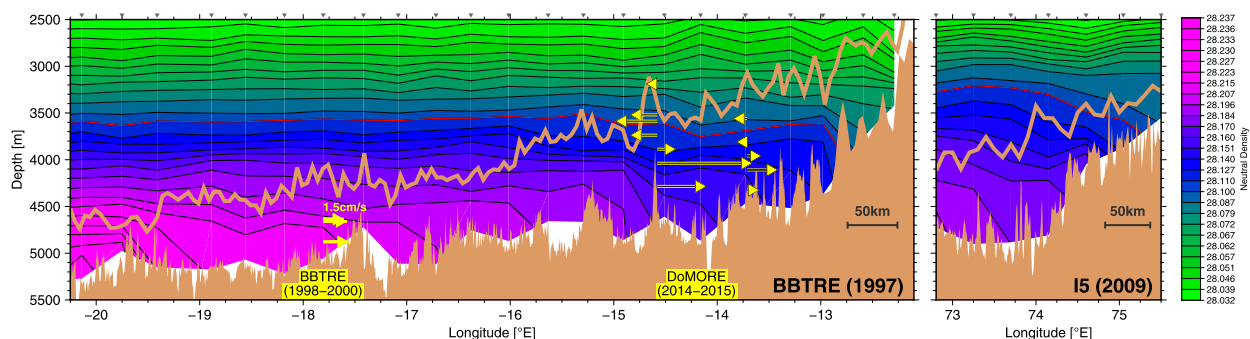
FIG. 3. Along-valley hydrography in two FZs; profile locations (see also Fig. 1) are marked with triangles above the panels. Valley topography—thalweg and crest depth of the shallower of the two sidewalls—is shown with tan color; the main shading and contours show neutral density, with the red contour marking the 28.11 surface proposed by de Lavergne et al. (2016) as the upper interface of AABW globally, and the remaining contour levels are spaced 100 m apart in the westernmost profile. (left) BBTRE hydrographic data from 1997 with 1- and 2-yr-averaged along-valley velocities recorded in 1996–98 (Thurnherr et al. 2005) and 2014–15 (Clément et al. 2017); current speeds $<0.005\,\mathrm{m\,s^{-1}}$ are not shown. (right) Arbitrary FZ sampled during the 2009 occupation of the I5 repeat-hydrography section across the Southeast Indian Ridge.
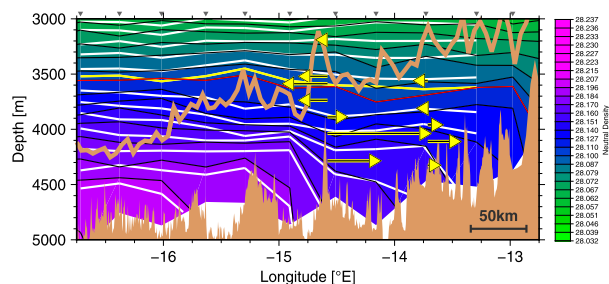
FIG. 4. Hydrography and along-valley flow in a stretch of FZ valley that was sampled at repeat stations in 1997 and 2015. Valley topography (tan color), neutral density observations from the 1997 survey (shading, black contours, and red AABW-NADW interface) and moored velocity data are plotted as in Fig. 3. Additional white contours show the same neutral density contours observed in 2014, with the yellow line indicating the corresponding AABW-NADW interface.

The hydrography along a 350-km-long stretch of the 21°S FZ was sampled in 1997 and 2014, and the density data from both surveys are shown superimposed in Fig. 4. The two samples are remarkably similar; in particular steep along-valley gradients occur in the same locations and have very similar magnitudes. This is consistent with prior inferences that the large-scale along-FZ density gradients are quasi-steady on time scales of decades (Thurnherr and Speer 2003), and that the locations of the steep along-valley density gradients in the FZ are locked to topography (Thurnherr et al. 2005). While the along-valley gradients have apparently not changed much between 1997 and 2014 the isopycnal surfaces inside the FZ show a consistent downward displacement that is likely related to large-scale climatic trends (Zhao and Thurnherr 2018). The mean horizontal density gradient along the 21°S FZ is on the order of $10^{-7}\,\mathrm{kg\,m^{-3}\,m^{-1}}$ (Thurnherr et al. 2005), and quasi-steady along-FZ density gradients of similar magnitude occur in all FZs on the MAR in the South Atlantic (Thurnherr and Speer 2003). Together, these observations indicate that the data from the 21°S FZ can be considered representative not only for long time scales but also for the many FZ valleys in this region. This inference leads to an estimate of 1.5–3 Sv of total AABW transformation and upwelling in the FZs on the western MAR flank in the Brazil basin, consistent with previous estimates (St. Laurent et al. 2001b; Morris et al. 2001).

During the 2014 survey, the cross-valley hydrography of the 21°S FZ was sampled at two different locations with high-resolution tow-yo casts. Figure 5 shows neutral density across a narrow stretch of the FZ near 14°7′W. Away from the immediate vicinity of the topography the density surfaces slope upward toward the north, which implies an increase with depth of the
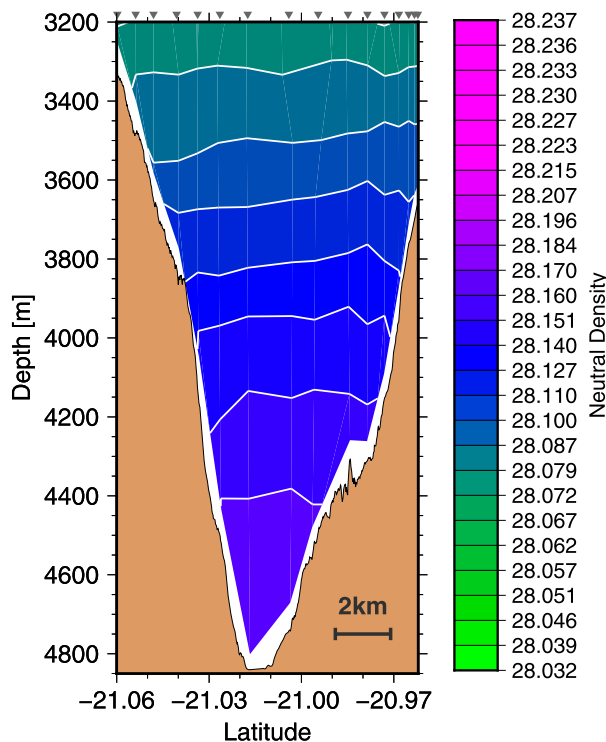
FIG. 5. Cross-valley neutral density section near 14°07′W.

eastward (semi)geostrophic zonal flow in this Southern Hemisphere valley. The cross-valley density gradients in this section are consistent with approximately $0.08\,\mathrm{m\,s^{-1}}\,(600\,\mathrm{m})^{-1}$ eastward shear between 3400 and 4000 m, similar to the shear in 1-yr-averaged velocities recorded in the DoMORE overflow (Fig. 3b in Clément et al. 2017). A second cross-valley section occupied at the DoMORE overflow shows similar cross-valley sloping isopycnals, although with much greater vertical excursions in the interior of the valley (Fig. 3a in Clément et al. 2017). The density surfaces at the upper interface of the eastward up-valley mean flow ($\approx$3900 m; Clément et al. 2017) slope upward toward the north across the entire width of the valley, indicating that the eastward flow fills the entire valley at both locations. In the cross section shown in Fig. 5, the valley is narrow ($\approx$8 km at the upper interface of the up-valley flow) relative to the local deformation radius $Nh/|f| \approx 13$ km, where $N \approx 7 \times 10^{-4}$ rad s^{-1} is the mean buoyancy frequency below 3900 m, $h = 1000$ m is the vertical extent of the up-valley flow, and $f = -5.2 \times 10^{-5}$ rad s^{-1} is the Coriolis parameter at 21°S. A similar calculation carried out in the DoMORE overflow yields the same conclusion (Clément et al. 2017), consistent with the isopycnals sloping upward toward the north extending across the entire valley at that site as well.

We are not aware of many FZ surveys outside the Atlantic Ocean. MacKinnon et al. (2008) describe

strong northward flow of AABW and high levels of mixing in the Atlantis II FZ, one of the prominent valleys crossing the Southeast Indian Ridge near 57°W. Similar to the Romanche and Chain FZs in the tropical Atlantic, the Atlantis II FZ provides a deep conduit across the ridge, whereas the 21°S FZ terminates near the MAR crest. The only other hydrographic section along a closed FZ valley that we are aware of is from the Southwest Indian Ridge near 74°E, a portion of which was surveyed during the 2009 occupation of the I5 repeat-hydrography section (Fig. 3, right panel). The similarities between the density fields in the South Atlantic and the Southwest Indian Ridge FZs are striking and imply similar dynamics, which suggests that FZs are likely important for transformation and upwelling of AABW wherever there are slow-spreading midocean ridges.

3. Fracture zone turbulence and mixing

To maintain a quasi-steady along-valley mean flow down a mean density gradient, turbulent mixing is required (St. Laurent et al. 2001b; Thurnherr et al. 2002). Ignoring temporal variability and nonlinearities in the seawater equation of state (McDougall 1991) the advection–diffusion equation for density, averaged on time and space scales larger than those associated with individual overturning events, is

$$u\rho_x + v\rho_y + w\rho_z = (\kappa\rho_x)_x + (\kappa\rho_y)_y + (\kappa\rho_z)_z, \quad (1)$$

where u, v, and w are the three Cartesian velocity components, κ is the eddy diffusivity of mechanical isotropic turbulence, ρ denotes density, and subscripts indicate partial derivatives. When applied to scales such as the ones considered here, horizontal eddy fluxes are typically ignored (e.g., Polzin et al. 1997; Kunze et al. 2012), which yields

$$u\rho_x + v\rho_y + w\rho_z \approx (\kappa\rho_z)_z. \quad (2)$$

Under these assumptions, advection of density is balanced by the vertical divergence of the turbulent vertical density flux $-\kappa\rho_z$ This density flux is closely related to the vertical flux of buoyancy $B = -g(\rho - \rho_0)/\rho_0$, where ρ_0 and g are a reference density and the acceleration due to gravity, respectively. In particular, the turbulent vertical density flux is proportional to the turbulent vertical buoyancy flux

$$F^T = -\kappa N^2 = \frac{g}{\rho_0}(\kappa\rho_z), \quad (3)$$

where N is the buoyancy frequency. Combining Eqs. (2) and (3) yields

$$u\rho_x + v\rho_y + w\rho_z \approx \frac{\rho_0}{g}(F^T)_z, \quad (4)$$

which, using the Osborn (1980) model to relate the vertical buoyancy flux to the more easily measurable dissipation of turbulent kinetic energy ε, becomes (e.g., Polzin et al. 1997)

$$u\rho_x + v\rho_y + w\rho_z \approx -\frac{\rho_0}{g}(\Gamma\varepsilon)_z, \quad (5)$$

where the parameter $\Gamma = -F^T/\varepsilon$, which is closely related to the mixing efficiency, indicates the ratio of buoyancy flux to energy dissipated. The small magnitude of the mean cross-valley horizontal velocities in the 21°S FZ (e.g., Fig. 2 in Thurnherr et al. 2005) indicates that the advection term involving y can be dropped when Eq. (5) is applied in a horizontally rotated coordinate frame where x is aligned with the valley. Since the available observations indicate mean along-valley flow down the density gradient and mean vertical upwelling (section 2) the remaining two advective terms $u\rho_x$ and $w\rho_z$ are both negative, implying that $(\Gamma\varepsilon)_z > 0$ is required for transformation of water from higher to lower densities (e.g., Polzin et al. 1997; St. Laurent et al. 2001b; Ferrari et al. 2016). Based on the mean along-valley and vertical density gradients ($\rho_x \approx -10^{-7}\,\mathrm{kg\,m^{-3}\,m^{-1}}$ and $\rho_z \approx -10^{-4}\,\mathrm{kg\,m^{-3}\,m^{-1}}$), the mean along-valley velocity away from overflows ($u \approx 2 \times 10^{-2}\,\mathrm{m\,s^{-1}}$), as well as the mean upwelling velocity estimated in section 2 ($w \approx 2 \times 10^{-5}\,\mathrm{m\,s^{-1}}$) we infer approximately equal contributions from horizontal and vertical advection of density.

Vertical profiles of ε in and around the Brazil basin FZ valley near 21°S were collected in 1997 (Polzin et al. 1997; St. Laurent et al. 2001b) and in 2015 (Clément et al. 2017). Both datasets reveal high levels of spatial patchiness and temporal intermittency. Lacking knowledge of the detailed distribution of turbulence in time and space, we rely on statistical descriptions (models) of "mean" turbulence levels at a given site. Because of the close link between bottom-generated internal waves and turbulence in regions of rough topography, such models are often based on turbulence measurements averaged in height-above-bottom coordinates (e.g., St. Laurent et al. 2001b; Polzin 2009), even though this choice obscures local turbulence maxima from processes that are not locked to the seafloor (Clément and Thurnherr 2018).

Figure 6 shows height-above-bottom averaged turbulence profiles from both microstructure surveys. The DoMORE data were split into two subsets (Clément et al. 2017): one with the data collected in and around a hydraulically controlled overflow and the other with all
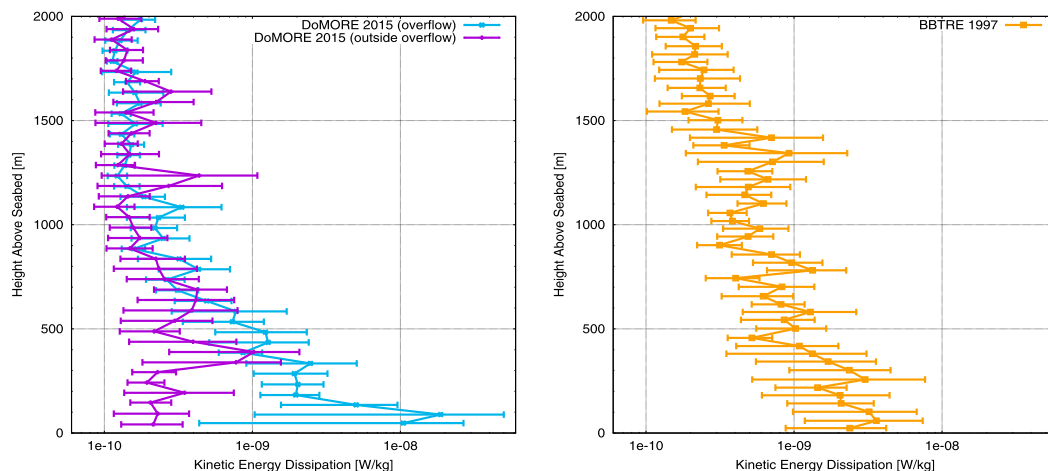
FIG. 6. Height-above-bottom-averaged profiles of turbulent kinetic energy dissipation in FZ valleys on the western flank of the MAR near 21°S; error bars show 95% confidence intervals from bootstrapping. (left) From the 2015 DoMORE survey of the 21°S FZ (Clément et al. 2017). (right) From all FZ profiles (about one-half in the 21°S FZ) in the 1997 BBTRE survey of the western MAR flank between 21° and 24°S (St. Laurent et al. 2001b).

remaining profiles. Both the overflow profile and the BBTRE mean profile show local maxima approximately 100 m above the seabed, although the downward decrease below this peak is not statistically significant in either. Above these near-bottom turbulence maxima ε decreases with height at least up to 2000 m above bottom (mab), where the turbulence levels reach "background" values. The apparent differences between the turbulence levels observed during BBTRE and DoMORE are due to a combination of temporal and spatial variability in the turbulence field. The noise level of the dissipation rate varies due to technical differences between the two microstructure instruments used for the surveys. As discussed in the appendix, the noise level of the dissipation rate also depends on spectral corrections applied during data processing.

The mean DoMORE dissipation profile outside the overflow is qualitatively different from the mean overflow and BBTRE profiles, with a more pronounced turbulence maximum hundreds of meters above the seabed and approximately uniform ε levels below. Inspection of the underlying profiles indicates that that the local maximum in the mean profile 300–400 m above the seabed is caused by turbulence maxima near 4000 m, which coincides with the depth of the shear layer at the top of the up-valley flow (Clément et al. 2017). We therefore conclude that the local dissipation maximum in the mean DoMORE dissipation profile outside the overflow is likely related to wave-mean flow interaction in the FZ valley as documented by Clément and Thurnherr (2018).

The mean along-flow buoyancy gain observed inside FZ valleys (section 2) implies convergence of the turbulent buoyancy flux at all depths below the crests of the lateral valley walls. Noting also that eastward density decrease over the western flank of the MAR in the Brazil basin is largely restricted to the insides of the FZ valleys (Thurnherr and Speer 2003), we follow Kunze et al. (2012) and hypothesize that the valley topography must play an important role. As parameterized in the density Eq. (1), turbulence causes downward buoyancy fluxes in regions of stable stratification. Thus, the buoyancy fluxes integrated along arbitrary paths between the two valley walls must be consistently downward as well. The magnitudes of such cross-valley integrated buoyancy fluxes depend on the amount of mixing along the integration paths, with both pathlength and turbulence levels affecting the integrals. When considering two different depths in a stably stratified valley (or in a depression of another convex shape) with downward increasing turbulence levels, two opposing effects affect the cross-valley integrated buoyancy fluxes: (i) the turbulence levels are higher on the lower isobath, which is closer to the seabed, and (ii) the integration path along the lower isobath is shorter.

The two effects capture the opposite contributions of interior and boundary fluxes to the buoyancy flux divergence integrated between the valley walls in this model: the interior fluxes are generally divergent (implying conversion to higher densities), while the fluxes within the bottom boundary layers are convergent (implying conversion to lower densities) because the flux must drop to zero at the seabed. While both effects have been considered separately before—$\partial \varepsilon / \partial z < 0$ by Polzin et al. (1997) and valley hypsography (effect ii)

by Kunze et al. (2012)—the combined effects have apparently not been investigated yet. Based on the hydrographic observations presented in section 2, it is anticipated that inside FZ valleys the hypsographic effect or equivalently the bottom boundary flux convergence dominates, consistent with inferences from idealized studies (Polzin 2009; Ferrari et al. 2016).

To test this inference, as well as to assess the potential importance of geothermal heating in this setting, profiles of cross-valley integrated turbulent buoyancy flux

$$F_{\text{int}}^T(x,z) = \int F^T(x,y,z)\,dy \approx -\Gamma \int \varepsilon(x,y,z)\,dy, \qquad (6)$$

where y is aligned with the cross-valley direction, are derived. For simplicity, Γ is assumed to be constant with the conventional value of 0.2, and it is also assumed that a single height-above-bottom (hab) dissipation profile applies uniformly across the valley. The three ε(hab) profiles shown in Fig. 6 are tested; all profiles are extended above 2000 mab with constant values corresponding to the approximate background turbulence level $(2 \times 10^{-10}\,\text{W kg}^{-1})$. Below the bottommost dissipation measurements, the turbulent buoyancy flux is linearly interpolated to zero at the seabed, where it must vanish (Ferrari et al. 2016). Note that the net buoyancy flux convergence in the bottom boundary layer does not depend on the vertical structure chosen for this interpolation, which only affects the vertical ''smoothness'' of the numerical solutions discussed below. Rather, it only depends on the turbulent buoyancy flux entering the boundary layer from above.

The calculations are carried out at 10-m vertical resolution with valley cross sections taken from a 200-km-long stretch of FZ where multibeam bathymetry covering the valley floor and part of both sidewalls are available (Fig. 2). The global ETOPO-1 dataset, which has an effective horizontal resolution of approximately 10 km, is used to extend the topographic coverage up to the crests of the sidewalls. Figure 7 shows two cross-valley topographic sections, as well as the corresponding profiles of the cross-valley integrated turbulent buoyancy fluxes $F_{\text{int}}^T(z)$. For all three ε(hab) profiles, the hypsographic effect exceeds the vertical divergence of the turbulent buoyancy fluxes inferred from the vertical gradients of dissipation inside the FZ, resulting in net downward-decreasing integrated buoyancy fluxes below the crests of the lateral valley walls. Equivalently, this means that the transformation to lighter densities in the layer of strong buoyancy flux convergence along the boundaries dominates over the densification in the interior where $\partial\varepsilon/\partial z < 0$. The magnitudes of the

turbulent buoyancy fluxes and their convergences depend sensitively on the ε profiles used in the calculations. The difference in magnitude between the two DoMORE estimates is qualitatively consistent with a strong association between sills and along-valley density gradients in the 21°S FZ (Thurnherr et al. 2005). The vertical smoothness of the individual solutions at each site is strongly affected by the vertical scale of the buoyancy-convergence region, that is, primarily by the distance of the ε maximum from the seabed.

The buoyancy-flux maxima in the profiles shown in Fig. 7 are estimates of the total buoyancy that is fluxed downward by turbulence into the FZ at the two locations. (Since buoyancy fluxes vanish at the bottom of the valley they also serve as estimates for the vertically integrated buoyancy-flux convergences at the two sites.) Dividing by the distance between the crests of the sidewalls yields turbulent buoyancy fluxes per unit area, which can be compared to the buoyancy effects of geothermal heating. In the area shown in Fig. 2 the mean turbulent buoyancy flux into the valley derived from the DoMORE overflow dissipation profile is $1.2 \times 10^{-9}\,\text{m}^2\,\text{s}^{-3}$, more than an order of magnitude higher than the corresponding estimate from the nonoverflow profile $(8 \times 10^{-11}\,\text{m}^2\,\text{s}^{-3})$. In the DoMORE microstructure survey region the overflow affects nearly 20% of the valley (Fig. 1b in Clément et al. 2017), which yields an area-weighted estimate for the mean turbulent buoyancy flux into the valley of $\approx 3 \times 10^{-10}\,\text{m}^2\,\text{s}^{-3}$. An order-of-magnitude estimate for the buoyancy flux per unit area due to geothermal heating F^G can be calculated from

$$F^G = \frac{\alpha_v g}{c_p \rho_0}\mathscr{G}, \qquad (7)$$

where $\alpha_v \approx 1.9 \times 10^{-4}\,\text{K}^{-1}$ is the volumetric temperature expansion coefficient for seawater in this environment, $c_p \approx 3900\,\text{J kg}^{-1}\,\text{K}^{-1}$ is the corresponding specific heat, and $\mathscr{G}$ is the geothermal heat flux. Based on the data presented in Fig. 5a of Davies (2013), $\mathscr{G} \approx 0.05\,\text{W m}^{-2}$ in our study region, which yields a buoyancy flux of $F^G \approx 2.5 \times 10^{-11}\,\text{m}^2\,\text{s}^{-3}$, that is, about an order of magnitude lower than the turbulent buoyancy flux from above. We conclude that geothermal heating does not play a significant role in the buoyancy budget of this FZ valley, which is consistent with the lack of a geothermal heating signal in the deep temperature/salinity properties. [For a different conclusion in the rift valley of the MAR, see Thurnherr et al. (2002).]

The example sections shown in Fig. 7 are representative for the entire FZ region (Fig. 2). In particular, there are cross-valley integrated turbulent buoyancy-flux
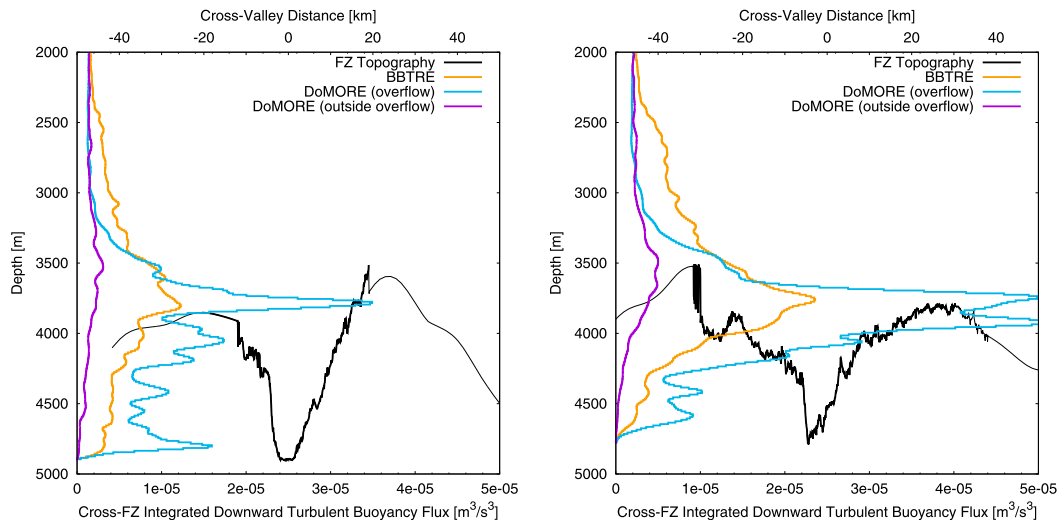
FIG. 7. Example valley cross sections and corresponding cross-valley integrated downward turbulent buoyancy fluxes, derived using the mean BBTRE and DoMORE dissipation profiles (Fig. 6): (left) near 14°55′W and (right) near 14°12′W. The ''e'' on the x axis indicates that the leading numeral should be multiplied by 10 raised to the trailing sign and numerals.

maxima associated with the crests of the lateral valley walls throughout the region, implying (i) turbulent transformation to lighter densities inside the valley, aided by geothermal heating across the seabed, and (ii) densification of the water above the depth of the sidewall crests. Since the MAR topography in the Brazil basin is in many ways typical for the flanks of slow-spreading ridges (Fig. 1), and since the along-valley density gradients observed in many FZs (section 2) require levels of diapycnal mixing similar to those in the 21°S FZ, we conclude that the inferences drawn from the Brazil basin data likely apply to other ocean basins bounded by slow-spreading midocean ridge flanks.

4. Discussion

Persistent unidirectional along-valley density gradients driving up-valley flows are a common feature of the abyssal FZs that corrugate the flanks of slow-spreading midocean ridges in large regions of the ocean (St. Laurent et al. 2001b; Thurnherr and Speer 2003; section 2). While such ''abyssal valley flows'' have been known for many years, the joint analysis of the BBTRE and DoMORE data carried out here provides support for two important prior inferences drawn from incomplete data: (i) the BBTRE and DoMORE data combined paint a consistent dynamical picture, in agreement with prior inferences of an approximate steady state on time scales from years to decades (Thurnherr and Speer 2003) and (ii) the distribution of the along-valley density gradients

observed during the BBTRE and DoMORE surveys is remarkably similar, consistent with the inference of Thurnherr et al. (2005) that the locations of strong water-mass transformation are topographically controlled.

An important goal of the present work is to show that there is no real contradiction between the *local* constraints on water-mass transformations from vertical convergence of turbulent buoyancy fluxes (Polzin et al. 1997) and the *integral* constraints arising from valley hypsography (Kunze et al. 2012). In particular, we point out that the model of Kunze et al. (2012) includes a well mixed bottom boundary layer beneath the interior stratified layer to which the model applies. As discussed in their paper, this well mixed boundary layer was not sufficiently sampled with microstructure to constrain the vertical gradients of the turbulent buoyancy fluxes near the seabed. However, while this is not explicitly discussed in their paper, the combination of a finite downward buoyancy flux at the top of this well stratified layer with the no-normal-flux boundary condition applied at the seabed (Kunze et al. 2012, p. 920) ensures net buoyancy-flux convergence in the well mixed boundary layer. We conclude that the buoyancy flux convergence that is required for the transformation to lighter densities in the model of Kunze et al. (2012) must take place entirely inside this weakly stratified boundary layer, consistent with the inferences of Ferrari et al. (2016).

In contrast to the simplified models considered by Kunze et al. (2012) and by Ferrari et al. (2016), the available observation from FZ valleys indicate regions

of buoyancy-flux convergence both in thin layers above the seabed (≈ 100 m in the data analyzed here), as well as in thicker layers associated with a hydraulically controlled overflow (Clément et al. 2017) and below critical layers that develop in the upper shear layer of the mean along-FZ flow (Clément and Thurnherr 2018). We conclude that there are a variety of different processes giving rise to layers with downward-decreasing dissipation where water in FZ valleys is transformed locally to lower densities. Additionally, it seems likely that the inhomogeneous distribution of turbulence in the FZs also creates significant horizontal gradients in the valley hydrography.

Another important conclusion arising from our work is the importance of valley hypsography in shaping the net bottom-water transformation to lighter densities. While the no-flux bottom boundary condition ensures that there is a layer of buoyancy convergence along the seafloor in any setting (Ferrari et al. 2016; McDougall and Ferrari 2017), our work confirms and generalizes the inference of Kunze et al. (2012) that it is the hypsography that controls the net downward decrease of the turbulent buoyancy fluxes inside submarine valleys. Essentially, the topography insulates the valley water from the surrounding, which implies that the entire buoyancy that is fluxed downward into valleys by turbulence must converge below the sidewall crests, with geothermal heating providing additional buoyancy to the same water. Our observations indicate little sensitivity of this effect to the vertical gradients in the turbulence profiles. In the context of numerical modeling, the inference that cross-valley integrated buoyancy flux convergence extends all the way from the valley thalweg to the crest depths of the sidewalls, with little dependence on the vertical structure of the turbulence profiles, leads to the welcome conclusion that bottom-water transformation is more sensitive to the representation of FZ valleys than to the shape of the turbulence profiles causing the mixing. In addition to sufficiently fine grids to resolve the FZ valleys, realistic transformation and upwelling of bottom water in models requires accurate representation of the turbulent buoyancy fluxes into the valleys.

The inference that valley hypsography controls the transformation of bottom water to lighter densities in FZs is consistent with the large-scale hydrographic and velocity observations from the 21°S valley (section 2), which we consider representative for the corresponding cross-valley averages. Support for this assumption is provided by the observation that the cross-FZ density field away from the immediate vicinity of the topography is approximately uniform (Fig. 5) and also that there is evidence for the deep up-valley currents filling the entire width of the valley (Clément et al. 2017). The observation that the valley hydrography is laterally well mixed requires vigorous horizontal stirring of the horizontal hydrographic gradients, which is clearly important for a detailed understanding of the buoyancy pathways in FZ valleys. Similar to others (e.g., Kunze et al. 2012), we have not found a way to constrain the lateral turbulent fluxes from our data.

As stated in section 2, the 1.5–3 Sv of water that are transformed and upwelled in FZ valleys on the western MAR flank in the Brazil basin are sufficient to balance the total inflow of AABW into the basin; that is, there is no need for transformation and upwelling of AABW anywhere else in the basin. FZ valleys are not just found in the Brazil basin (Fig. 1), with the observations from a random FZ valley in the Indian Ocean supporting the inference that similar water mass transformation and upwelling takes place in most or all FZ valleys. Since midocean ridges rise from abyssal basins below 5000 m and typically reach crest depths of ≈ 2000 m we conclude that most FZ valleys are filled with AABW. Based on the estimates given in section 1, FZ valleys in the Brazil basin account for $\approx 5\%$ of the global total axial length, implying that FZ valleys can transform and upwell 30–60 Sv of bottom water globally. Since this is sufficient to account for the entire northward transport of AABW across 30°S (de Lavergne et al. 2016), where this transport reaches a maximum, we conclude that the global AABW orverturning cell is closed primarily in FZ valleys.

Beyond FZs and other abyssal valleys (e.g., Thurnherr et al. 2002), the arguments presented in section 3 apply also to topographically closed depressions of arbitrary shape, as long as the assumption of horizontally uniform ε(hab) across the depressions is approximately correct (i.e., as long as the depressions are not very large). Below the rims of closed depressions, hypsography causes a tendency for convergence of the horizontally averaged turbulent buoyancy fluxes extending all the way from the bottom to the rim depths, which together with geothermal heating ensures lightening of any dense water topographically blocked inside. (Of course, local transformation to lighter densities is confined to regions where $\partial \varepsilon / \partial z > 0$.) Because the blocked water is continuously gaining buoyancy, it is displaced upward (causing upwelling) by laterally inflowing denser water. Thus, the arguments put forward in this paper also help explain why isolated depressions in the abyssal ocean are not typically filled with stagnant water.
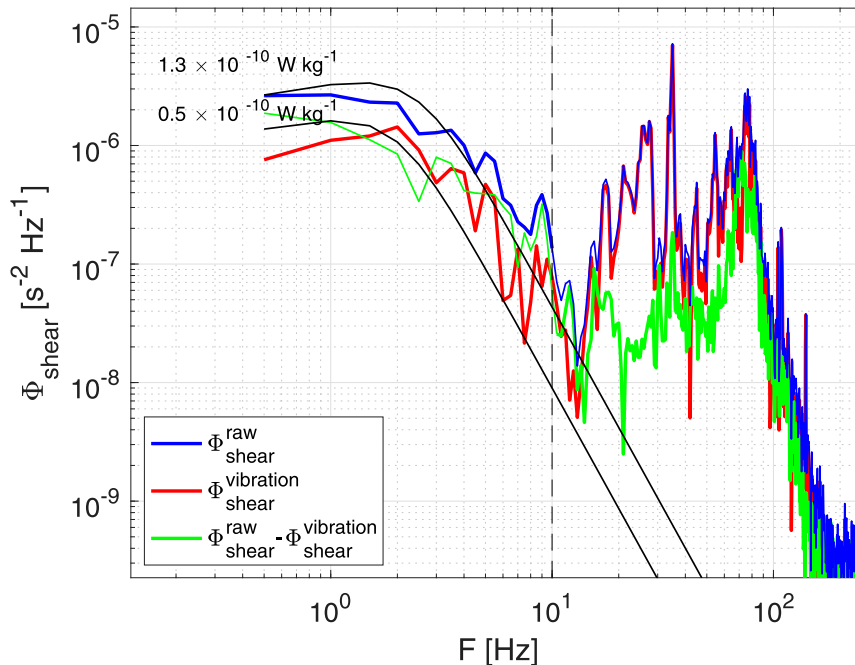
FIG. A1. Sample of shear spectra with and without the Goodman correction (green and blue, respectively) together with the corresponding vibration-coherent shear spectrum (red), from DoMORE RVMP data.

APPENDIX

Vehicle Vibration Treatment for the TKE Dissipation Estimate

Airfoil probes are well known to be highly sensitive to vehicle vibrations. Apparent noise peaks can be found in shear spectra at frequencies above about 10 Hz both from the High Resolution Profiler (HRP; Polzin and Montgomery 1996), used in BBTRE, and from the Rockland VMP-6000 (RVMP; blue line in Fig. A1), used in DoMORE. In the HRP system, dissipation rates were estimated by integrating shear spectra up to a wavenumber of a local spectral minimum to avoid the inclusion

of such apparent peaks (Polzin and Montgomery 1996). In the RVMP system, on the other hand, high-frequency vehicle vibrations are concurrently sensed through multiaxis analog accelerometers, which allows removing vibration-coherent signals from the shear spectra using the method of Goodman et al. (2006). In the Rockland processing software the Goodman correction is by default applied over the entire frequency range. While this correction successfully removes apparent high-frequency noise peaks (green line in Fig. A1), the resulting mean DoMORE turbulence levels are about an order of magnitude lower than the corresponding BBTRE levels (not shown). Inspection of the spectra at frequencies below 10 Hz indicates that a significant low-frequency portion of shear signals is also coherent with vibrations, particularly, in quiet oceanic conditions $\varepsilon \sim O(10^{-10})\mathrm{W\,kg^{-1}}$. As, furthermore, such vibration-coherent low-frequency shear spectra often follow the Nasmyth universal spectral form (Wolk et al. 2002; black lines in Fig. A1), we infer that the Goodman correction applied to frequencies below 10 Hz likely causes excessive removal of real oceanic turbulence signals and leads to underestimates of the dissipation rate, especially in quiet oceanic conditions. We therefore did not apply this correction at frequencies less than 10 Hz for the DoMORE dissipation estimates, resulting in good agreement between the BBTRE and DoMORE turbulence levels (Fig. 6).

REFERENCES

Armi, L., 1979: Effects of variations in eddy diffusivity on property distributions in the oceans. *J. Mar. Res.*, **37**, 515–530, http://doi.org/10.1575/1912/10336.

Clément, L., and A. M. Thurnherr, 2018: Abyssal upwelling in mid-ocean ridge fracture zones. *Geophys. Res. Lett.*, **45**, 2424–2432, https://doi.org/10.1002/2017GL075872.

——, ——, and L. C. St. Laurent, 2017: Turbulent mixing in a deep fracture zone on the Mid-Atlantic Ridge. *J. Phys. Oceanogr.*, **47**, 1873–1896, https://doi.org/10.1175/JPO-D-16-0264.1.

Davies, J. H., 2013: Global map of solid earth surface heat flow. *Geochem. Geophys. Geosyst.*, **14**, 4608–4622, https://doi.org/10.1002/ggge.20271.

de Lavergne, C., G. Madec, J. Le Sommer, A. J. G. Nurser, and A. C. Naveira Garabato, 2016: On the consumption of Antarctic Bottom water in the abyssal ocean. *J. Phys. Oceanogr.*, **46**, 635–661, https://doi.org/10.1175/JPO-D-14-0201.1.

Ferrari, R., A. Mashayek, T. J. McDougall, M. Nikurashin, and J.-M. Campin, 2016: Turning ocean mixing upside down. *J. Phys. Oceanogr.*, **46**, 2239–2261, https://doi.org/10.1175/JPO-D-15-0244.1.

Goodman, L., E. Levine, and R. G. Lueck, 2006: On measuring the terms of the turbulent kinetic energy budget from an AUV. *J. Atmos. Oceanic Technol.*, **23**, 977–990, https://doi.org/10.1175/JTECH1889.1.

Klocker, A., and T. J. McDougall, 2010: Influence of the nonlinear equation of state on global estimates of dianeutral advection and diffusion. *J. Phys. Oceanogr.*, **40**, 1690–1709, https://doi.org/10.1175/2010JPO4303.1.

Kunze, E., C. MacKay, E. E. McPhee-Shaw, K. Morrice, J. B. Girton, and S. R. Terker, 2012: Turbulent mixing and exchange with interior waters on sloping boundaries. *J. Phys. Oceanogr.*, **42**, 910–927, https://doi.org/10.1175/JPO-D-11-075.1.

Ledwell, J. R., E. T. Montgomery, K. L. Polzin, L. C. St. Laurent, R. W. Schmitt, and J. M. Toole, 2000: Evidence for enhanced mixing over rough topography in the abyssal ocean. *Nature*, **403**, 179–182, https://doi.org/10.1038/35003164.

MacKinnon, J. A., T. M. S. Johnston, and R. Pinkel, 2008: Strong transport and mixing of deep water throug the Southwest Indian Ridge. *Nat. Geosci.*, **1**, 755–758, https://doi.org/10.1038/ngeo340.

McDougall, T. J., 1991: Parameterizing mixing in inverse models. *Dynamics of Oceanics Internal Gravity Waves: Proc. Sixth. 'Aha Huliko'a Hawaiian Winter Workshop*, Honolulu, HI, University of Hawai'i at Mānoa, 355–386.

——, and R. Ferrari, 2017: Abyssal upwelling and downwelling driven by near-boundary mixing. *J. Phys. Oceanogr.*, **47**, 261–283, https://doi.org/10.1175/JPO-D-16-0082.1.

Morris, M. Y., M. M. Hall, L. C. St. Laurent, and N. G. Hogg, 2001: Abyssal mixing in the Brazil Basin. *J. Phys. Oceanogr.*, **31**, 3331–3348, https://doi.org/10.1175/1520-0485(2001)031<3331:AMITBB>2.0.CO;2.

Osborn, T. R., 1980: Estimates of the local rate of vertical diffusion from dissipation measurements. *J. Phys. Oceanogr.*, **10**, 83–89, https://doi.org/10.1175/1520-0485(1980)010<0083:EOTLRO>2.0.CO;2.

Polzin, K. L., 2009: An abyssal recipe. *Ocean Modell.*, **30**, 298–309, https://doi.org/10.1016/j.ocemod.2009.07.006.

——, and E. T. Montgomery, 1996: Microstructure profiling with the high resolution profiler. *Proc. ONR Workshop on Microstructure Sensors*, Mt. Hood, OR, Office of Naval Research, 109–115.

——, J. M. Toole, J. R. Ledwell, and R. W. Schmitt, 1997: Spatial variability of turbulent mixing in the abyssal ocean. *Science*, **276**, 93–96, https://doi.org/10.1126/science.276.5309.93.

St. Laurent, L. C., J. M. Toole, and R. W. Schmitt, 2001a: Mixing and diapycnal advection in the ocean. *From Stirring to Mixing in a Stratified Ocean: Proc. 12th 'Aha Huliko'a Winter Workshop*, Honolulu, HI, University of Hawai'i at Mānoa, 175–185.

——, ——, and ——, 2001b: Buoyancy forcing by turbulence above rough topography in the abyssal Brazil Basin. *J. Phys. Oceanogr.*, **31**, 3476–3495, https://doi.org/10.1175/1520-0485(2001)031<3476:BFBTAR>2.0.CO;2.

Thurnherr, A. M., and K. G. Speer, 2003: Boundary mixing and topographic blocking on the Mid-Atlantic Ridge in the South Atlantic. *J. Phys. Oceanogr.*, **33**, 848–862, https://doi.org/10.1175/1520-0485(2003)33<848:BMATBO>2.0.CO;2.

——, K. J. Richards, C. R. German, G. F. Lane-Serff, and K. G. Speer, 2002: Flow and mixing in the rift valley of the Mid-Atlantic Ridge. *J. Phys. Oceanogr.*, **32**, 1763–1778, https://doi.org/10.1175/1520-0485(2002)032<1763:FAMITR>2.0.CO;2.

——, L. C. St. Laurent, K. G. Speer, J. M. Toole, and J. R. Ledwell, 2005: Mixing associated with sills in a canyon on the mid-ocean ridge flank. *J. Phys. Oceanogr.*, **35**, 1370–1381, https://doi.org/10.1175/JPO2773.1.

Toole, J. M., 2007: Temporal characteristics of abyssal finescale motions above rough bathymetry. *J. Phys. Oceanogr.*, **37**, 409–427, https://doi.org/10.1175/JPO2988.1.

Wolk, F. H., H. Yamazaki, L. Seuront, and R. G. Lueck, 2002: A new free-fall profiler for measuring biophysical microstructure. *J. Atmos. Oceanic Technol.*, **19**, 780–793, https://doi.org/10.1175/1520-0426(2002)019<0780:ANFFPF>2.0.CO;2.

Zhao, J., and A. M. Thurnherr, 2018: Changes in bottom water physical properties above the Mid-Atlantic Ridge flank in the Brazil Basin. *J. Geophys. Res. Oceans*, **123**, 708–719, https://doi.org/10.1002/2017JC013375.